# Molecular biosensor based on a coordinated iron complex

Karim Salazar-Salinas,[1] Luis A. Jauregui,[1] Carlos Kubli-Garfias,[1,a)] and Jorge M. Seminario[1,2,b)]
[1]*Department of Chemical Engineering, Texas A&M University, College Station, Texas 77843-3122, USA*
[2]*Department of Electrical and Computer Engineering, Texas A&M University, College Station, Texas 77843-3122, USA*

(Received 6 October 2008; accepted 22 December 2008; published online 9 March 2009)

A sensor model based on the porphyrin nucleus of the soluble guanylate cyclase enzyme is modeled and tested with nitric oxide and carbon monoxide. Molecular oxygen is tested as a possible interferer. Geometries and electronic structures of the model are assessed by density functional theory. Vibrational circular dichroism (VCD), infrared, and Raman spectra are obtained for the iron complexes uncoordinated and coordinated with the gas moieties. The sensor is capable of detecting the ligands to different extents. Carbon monoxide is less detectable than nitric oxide due to the adopted position of the molecule in the sensor; carbon oxide is aligned with the iron atom, while nitric oxide and molecular oxygens bend with an angle detectable by the VCD. It is suggested that pollutants may be detected and measured with the proposed biosensors © *2009 American Institute of Physics*. [DOI: 10.1063/1.3070235]

## I. INTRODUCTION

Air pollutants produce adverse environmental and health effects. Some of them are highly reactive gases and they increase the toxicity of the air. Nitric oxide is a toxic compound generated by automobile engines and power plants.[1] Pollutants accumulation in the air causes acid rain; and, in mammal organisms, is associated with various carcinomas, deamination of DNA,[2] juvenile diabetes, multiple sclerosis, arthritis, and ulcerative colitis. Carbon monoxide displaces the oxygen from hemoglobin, interfering with oxygen transport.

Fortunately, living organisms have developed specific recognition mechanisms, through biomolecules, which represent ideal models for the study and design of sensors. In this effort, we use *in silico* techniques to evaluate the detection method of the molecular recognition, as electronic and vibrational properties. The biological model is the soluble guanylate cyclase (sGC) enzyme, a five-coordinated iron complex.[3] A conformational change permits the activation of the enzyme, in order to catalyze the cyclic guanosine 3′,5′-monophosphate formation.[4] Nitric oxide (NO)[5] and carbon monoxide (CO) activate sGC through the binding of the five coordinated iron complex. The sGC does not permit the access of $O_2$, and it shows more affinity to NO than to CO.[6] However, the molecular details of ligand discrimination and differential response to NO and CO are not well understood.

The gas sensor model is based on the five coordinated iron complex (5C);[7] taking advantage of the specific recognition by carbon monoxide (CO) and nitric oxide (NO) of the sGC in order to design a multifunctional sensor or host-guest chemistry with diversely coordinated central metals.[8] The complex is formed by porphyrin, which consists of four pyrrole rings linked by a methane bridge,[9] where the central position is occupied by a ferrous iron ($Fe^{+2}$), which is coordinated to nitrogen atoms from the pyrrole rings and one nitrogen from histidine axial ligand. We analyze the electronic and vibrational properties in order to distinguish the presence of CO, NO, and the interference of $O_2$ in our model. Recently, the magnetic field has been used to induce self-organization of porphyrin[10] during the condensation process of oligoporphyrins,[11] taking advantage of the strong interaction between the applied magnetic field and the ferrous porphyrin.[12] The study of ferrous porphyrin complexes is important because of its high potential in spintronics applications,[13] excellent tunable spectroscopic and spin valve[14] properties, potentially useful as sensors, molecular switches, optoelectronic devices, and antenna systems.[15]

## II. METHODOLOGY

The geometric structures are optimized for several spin configurations using density functional theory (DFT) with the program GAUSSIAN-03 (Ref. 16) using the B3PW91 hybrid functional. This functional is a combination of the Becke-3 (B3) (Ref. 17) exchange functional and the Perdew–Wang (PW91)[18–20] correlation functional. The B3 exchange functional uses the nonlocal Becke-88 functional plus an exchange component calculated similarly to Hartree–Fock, but uses the Kohn–Sham molecular orbitals (MOs) instead. The derivatives of the energy with respect to the Cartesian coordinates of all atoms are evaluated; the geometry is then modified in order to reach forces below a threshold assuring that the atomistic system is in equilibrium, i.e., forces are approximately zero in all atoms.[21] From a DFT calculation perspective, the electronic configuration for a system of atoms with unfilled *d* orbitals is difficult to treat computationally; because of the strong coupling between correlation and

a)Permanent address: Instituto de Investigaciones Biomédicas, Universidad Nacional Autónoma de México, Mexico.
b)Electronic mail: seminario@tamu.edu.

 

exchange effects. Partially, quasirelativistic pseudopotentials and basis set LANL2DZ as mentioned elsewhere[22] alleviates this problem.[23]

Geometry optimizations are followed by a second derivative calculation (frequencies) for two reasons: to determine the existence of a true local minimum and to detect the sensing capacity of our model. If negative eigenvalues are found in the Hessian matrix, the geometry is modified in order to drive the system into a true local minimum. Imaginary frequencies correspond to negative eigenvalues in the Hessian matrix, and are related to unstable geometrical conformations. The self-consistency of the noninteractive wave function is performed with a convergence threshold on the density matrix of $10^{-6}$ and $10^{-8}$ for the root mean square and maximum density matrix error between iterations, respectively.

Raman intensities require the evaluation of third derivatives of the total energy with respect to perturbations of the Cartesians coordinates of the nuclei $\vec{R}$ and of an external electric field $\vec{F}$; apart from a constant $k$, the Raman intensity can be written as[24]

$$I_{\mathrm{Raman}} = k\left(\frac{\partial^3 E}{\partial \vec{R}\,\partial \vec{F}^2}\right)^2. \tag{1}$$

This equation requires the use of both occupied and unoccupied MOs, since $E$ is a sum of the integrals with corresponding derivatives have been calculated analytically; those that include DFT exchange-correlation terms are calculated numerically on a grid. The DFT infrared (IR) intensities are calculated from the dipole moment derivatives; while polarizability derivatives for Raman activities are obtained using numerical differentiation of the analytic dipole moment derivatives with respect to the applied electric field.

The vibrational circular dichroism (VCD) signal results from the differential absorption of left and right circularly polarized infrared lights during a vibrational transition of a chiral molecule. The B3PW91 functional results are comparable with the experimental data. The difference of absorption between left and right circularly polarized lights is proportional to the rotational strength ($R_{fi}$), imaginary part of the scalar product of the electric and magnetic dipole transition moments between the initial state $i$ and the final state $f$.[25]

$$R_{fi} = \mathrm{Im}\{\langle i|\mu|f\rangle\langle f|m|i\rangle\}, \tag{2}$$

where $\mu$ is the dipole moment operator and $m$ is the magnetic dipole operator. In the vibrational transition calculus, the prediction of electric and magnetic dipole transition moments, within harmonic approximation, requires the harmonic force field (HFF), the atomic polar tensor and the atomic axial tensor. The inclusion of electron correlation effects, especially in calculations of HFFs, is of major importance for agreement between calculated and experimental spectra.[26] The procedure calculating vibrational rotational strength and VCD spectra using DFT, implemented in GAUSSIAN 03, was developed and described by Cheesemann *et al.* where the magnetic field-dependent basis functions, specifically gauge-invariant (including) atomic orbitals, are incorporated in DFT calculation of nuclear magnetic shielding tensor.[27]

The current-voltage characteristic ($I$-$V$) is used to discriminate among ligands, thus we calculate it for defining the signature of the sensing extent of our model. The ferrous porphyrin histidine complex is optimized with gold atoms in orthogonal position by binding through an organic thiol group. The effect of the bulk on the finite cluster is considered through a combination of Green function with DFT approach to determine the electrical characteristics of single molecule trapped at metal or semiconductor junctions. This procedure has been intensively developed[28] and adapted also for the study of reactions on surfaces.[29] The procedure starts with a series of single point calculations of the extended molecule, including the applied bias electric field. The applied bias potential yields a displacement field which is included as the excitation in the Hamiltonian of the extended molecule, thus a displacement field is incorporated in the Hamiltonian for each point of the $I$-$V$ characteristic. The resulting response is the electric field strength is self-consistently calculated at each point of the current-voltage curve. Thus, each point of the $I$-$V$ curve corresponds to a full *ab initio* calculation. The Hamiltonian ($H_{\mathrm{KS}}$) and overlap matrices ($S$) for several electric fields are obtained and all depend on the applied bias voltage $V$,

$$H_{\mathrm{KS}}(V)\psi(V) = \varepsilon(V)S(V)\psi(V), \tag{3}$$

$$H_{\mathrm{KS}}(V) = \begin{bmatrix} H_{11}(V) & H_{1M}(V) & H_{12}(V) \\ H_{M1}(V) & H_{MM}(V) & H_{M2}(V) \\ H_{21}(V) & H_{2M}(V) & H_{22}(V) \end{bmatrix}. \tag{4}$$

In the Green's function approach, the Green's function of the standalone molecule, $G_M$, is obtained from the Hamiltonian $H$ and overlap $S$ matrices of the extended molecule for each applied electric field. Thus for an incoming electron of energy $E$,

$$G_M(E,V) = [ES_{MM}(E,V) - H_{MM}(E,V) - \Sigma_L(E,V) - \Sigma_R(E,V)]^{-1} \tag{5}$$

obtained from the full Green's function of the junction,

$$G(E,V) = \begin{bmatrix} g_1^{-1} & -\tau_1 & 0 \\ -\tau_1^{+} & ES_{MM}(V) - H_{MM}(V) & -\tau_2^{+} \\ 0 & -\tau_2 & g_2^{-1} \end{bmatrix}^{-1} \tag{6}$$

and

$$\Sigma_i(E,V) = (ES_{Mi} - H_{Mi})g_i(ES_{iM} - H_{iM}) \quad \text{for} \quad i = L,R, \tag{7}$$

where $\tau_i = (ES_{iM} - H_{iM})$ and $E$ is the transferred electron energy, $S_{MM}$ is the overlap matrix referred to the molecule, and $H_{MM}$ is the Hamiltonian of the standalone molecule obtained from GAUSSIAN 03 program with an electric field applied to the extended molecule. $\Sigma_i$ is the interaction between the contact $i$ and the standalone molecule; this self-energy term contributes to the shifting and the broadening of the molecular electronic levels and depends on Green's function $g_i$ describing the contacts.[30,31] The contact or nanocontacts to be pre-

cise are described explicitly by the following matrix:[32–34]

$$g_i(E) = \pi i \begin{bmatrix} g_{i1} & \cdots & 0 \\ \vdots & \ddots & \vdots \\ 0 & \cdots & g_{iN_i} \end{bmatrix}, \tag{8}$$

where the $i$ multiplying the matrix is the imaginary unit and should not be confused with the subscript indicating the left ($L$) and right ($R$) contacts for $i=2$ and for $i=1$, respectively. Each element $g_{iK}$ is given by

$$g_{iK} = \begin{bmatrix} (D_s)_{iK}(E) & 0 & 0 & 0 \\ 0 & (D_p)_{iK}(E) & 0 & 0 \\ 0 & 0 & (D_{d_{t_{2g}}})_{iK}(E) & 0 \\ 0 & 0 & 0 & (D_{d_{e_g}})_{iK}(E) \end{bmatrix}. \tag{9}$$

The diagonal values yield the $s$, $p$, $d_{t2g}$, and $d_{eg}$ contributions to the density of states ($D$) of each contact atom $K$. The number of contact atoms is such that the size of $g_i$ ($E$) equals the number of columns (rows) of the coupling matrix $H_{Mi}(H_{iM})$. For this particular work, all the $g_i(E)$ have been calculated for gold using the CRYSTAL program.[35]

The total density of state ($D$) of the standalone molecule absorbed to the contact is then obtained through a Green function approach, whereby the continuum broadens and shifts the discrete MOs of the complex. For further details regarding the theoretical methods used in this work, see Refs. 32–34 This bulk DOS $D$ is obtained using the GENIP program,[32]

$$D(E) = \mathrm{Tr}(i(G_M(E) - G_M^+(E))S_{MM}). \tag{10}$$

The transmission probability ($T$) is calculated as follows:[36]

$$T(E,V) = \mathrm{Trace}(\Gamma_L(E,V)G_M(E,V)\Gamma_R(E,V)G_M^+(E,V)), \tag{11}$$

where $\Gamma_i = i(\Sigma_j(E,V) - \Sigma_j^+(E,V))$ is the imaginary part of the self-energy, and $\Sigma_j$, $\Gamma_j$ represent the coupling between the contacts and the molecule, in general, $G^+$ is the adjoin of $G$, and $\Sigma_i(E) = \tau_i^+ g_i \tau_i$ for $j=1,2$. Generalizing the Landauer equation as a function of $V$,

$$I(V) = \frac{2e}{h}\int_{-\infty}^{\infty} T(E,V)[f_L(E - eV/2) - f_R(E + eV/2)]dE, \tag{12}$$

where $e$ is the charge of one electron, $h$ is Planck's constant, and $f_j(E,V_j)$ the Fermi–Dirac distribution of the Au tip at an electric potential $V_j$. Thus, the current through the junction depends on the Fermi level and the transmission function, as well as, the bias voltage applied to the system and the coupling of the pairs to the tips.

Equation (12) can be summarized to[37]

$$I \approx \frac{2e}{h}\int_{E_f+V_1}^{E_f+V_2} T(E,\Delta V)dE. \tag{13}$$

Two complexes are built to test the sensor, a ferrous porphyrin alone and a ferrous porphyrin histidine complex.

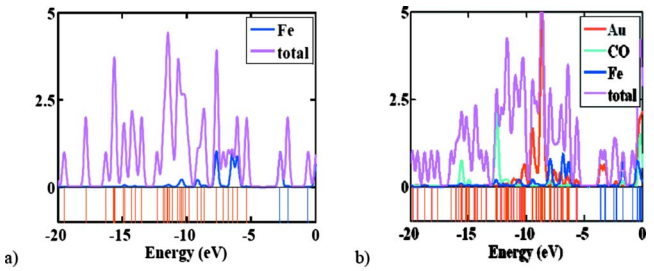


FIG. 1. (Color online) (a) Density of state of ferrous porphyrin complex **B** and (b) CO-ferrous porphyrin with gold atoms in orthogonal position **D**. The upper curves show total density of state (magenta), partial density of state of ferrous ion (blue), CO (cyan), and gold (red). The vertical lines depict the MO energies, unoccupied orbitals are shown in blue (right) and occupied orbitals in red (left).

The second optimized structure is our sensing gas model of nitric oxide (NO) and carbon monoxide (CO). The techniques for detection are based on IR, Raman, VCD frequencies, and current-voltage characteristics. Molecular oxygen ($O_2$) is considered as a possible interference, thus the detection method has to discriminate it. All these structures make junctions with a gold atom in an orthogonal position, with one upward and one downward electrodes with respect to the porphyrin. Therefore, the terminal hydrogen atoms of por-

TABLE I. Total and frontier orbitals energies of the ground state of (A) protoporphyrin (PP), (B) ferrous porphyrin (FeP), (C) ferrous porphyrin with gold atoms in orthogonal position (FeP-Au), and (D) carbon monoxide ferrous porphyrin with gold atoms in orthogonal position (CO–FeP–Au). Total energy is expressed in Hartrees (Ha) and frontier MO energies in eV.

| Molecule<br>Multiplicity<br>Energy(Ha)<br>HLG (eV) | HOMO (eV) | LUMO (eV) |
|---|---|---|
| A) PP<br>Singlet<br>-989.17844<br>2.91 | -5.25 | -2.34 |
| B) FeP<br>Triplet<br>-1111.54529<br>2.94 | -5.17 | -2.23 |
| C) FeP-Au<br>triplet<br>-2177.65464<br>1.96 | -5.58 | -3.62 |
| D) CO-FeP-Au<br>Singlet<br>-2290.92764<br>2.01 | -5.63 | -3.62 |

phyrin are substituted by the sulfur atoms to facilitate bonding to the gold electrodes. We use the basis set and effective core potentials LANL2DZ for gold and iron atoms, and the 6-31G(*d*) for the carbon, oxygen, nitrogen, hydrogen, and sulfur atoms.[38]

Practically all procedures are evaluated analytically, except those cases where the exchange-correlation integrals are involved; in this case, the calculation of the integrals for the entries in the Hamiltonian matrix is performed on a fine grid already tested to keep the tolerance of the used methods.

## III. RESULTS AND DISCUSSION

The CO adsorption effect on the electronic properties of Fe-porphyrin has been studied due to its role in living systems.[39] However, the model presents strong affinity to NO and $O_2$; the latter represents an important interference, which needs to be identified electronically spectroscopically.

### A. Fe-porphyrin

Ferrous porphyrin is analyzed with different multiplicities to determine its ground state. Table I shows the total energy: the highest occupied MO (HOMO) and the lowest unoccupied MO (LUMO) of the step by step porphyrin complexes (A–D) calculated using the B3PW91 functional with LANL2DZ basis set and effective core potentials for Fe and Au, and the 6-31G(*d*) basis set for C, N, and H.

As observed in Table I, (A) the HOMO and LUMO of protoporphyrin are located around the pyrrolic ring. In the case of ferrous porphyrin, (B) the HOMO maintains the cyclic shape and ferrous does not alter the delocalization of $\pi$-electrons; instead the LUMO is located as expected in the ferrous ion, adopting a typical *d* form. (C) Ferrous porphyrin with orthogonal gold atoms shows the HOMO also on the pyrrolic rings. Interestingly, the addition of the gold atoms changes the location of the LUMO from the ferrous ion to both gold atoms, yielding an iron atom with a poor contribution to the LUMO. (D) The presence of the CO ligand does not modify the location and shape of HOMO and LUMO; therefore, is expected that the *I-V* curve remains unmodified after the CO binding to the ferrous porphyrin.

Figure 1 shows the relationship between the density of states (*D*) and the distribution of MOs in both ferrous porphyrin (FeP) and CO-ferrous porphyrin with gold atoms in orthogonal position.

As observed ferrous contributes totally to the LUMO. The presence of the gold atoms reduces the bandgap because of their contribution to the LUMO. Interestingly, the carbon monoxide ligand does not alter the bandgap; therefore, the electrical behavior of the sensor model does not change notoriously with this exogenous ligand.

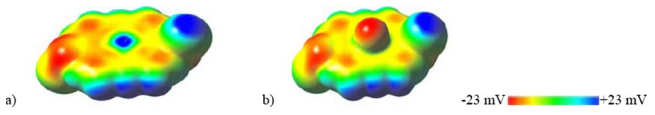


FIG. 2. (Color online) Molecular electrostatic potential of (a) ferrous porphyrin with gold orthogonal atoms **C** and (b) carbon monoxide ferrous porphyrin with orthogonal gold atoms **D**. The negativity of the CO group is observed in red.

Figure 2 shows the encoded (in color scale) molecular electrostatic potential of ferrous porphyrin (**C**) and CO-ferrous porphyrin (**D**), both have gold atoms at the ends as electrodes in orthogonal position.

The positive potential region on $Fe^{+2}$ permits binding with polar axial ligands NO or CO by accepting iron electrons into their empty ($\pi^*$) orbitals, i.e., backbonding.[40] It is expected that NO yields larger affinity because of its larger electronegativity.

### B. Characteristic of the Fe-porphyrin-histidine sensor model

The gas sensor consists of a ferrous ion coordinated to porphyrin and histidine (FeP-his). This model is tested with carbon monoxide, nitric oxide, and also molecular oxygen to analyze its interference capability.

#### *1. Ferrous complexes conformation*

Table II shows the total ground state energy of ferrous porphyrin histidine complex, FeP-his, C-his, with the ligands carbon monoxide, $D_1$-his, nitric oxide, $D_2$-his, and molecular oxygen $D_3$-his. These structures make a junction with a gold atom in an orthogonal position, one electrode upward and the other downward with respect to the porphyrin.

The most stable structure of the 5C iron complex has a multiplicity triplet (high spin), thus it has two unpaired electrons resulting in paramagnetic behavior. In 6C complexes the spin is lower; the multiplicity is doublet (NO) and singlet (CO and $O_2$). The high-spin state results from dispersion of 3*d* electrons to all orbitals and low-spin state is due to 3*d* electrons being restricted to low energy orbitals (triply degenerate $t_{2g}$ set).

Bond distances and angles change depending on the coordinated gas, yielding that the binding with the ferrous moiety is different for each case. Table III shows geometrical differences of the ligand and ferrous moieties.

TABLE II. Summary of the multiplicity states performed on the ferrous porphyrin histidine and its CO, NO, and $O_2$ complexes. Five coordinated complex (5C) and six coordinated complex (6C)

| | Coordination | Molecule | Multiplicity | Dipole moment (D) | Total energy (Ha) |
|---|---|---|---|---|---|
| **C**-his | 5C | FeP-his-Au | Triplet | 7.16 | −2650.996 81 |
| **D**$_1$-his | 6C | CO–FeP-his-Au | Singlet | 8.18 | −2764.286 84 |
| **D**$_2$-his | 6C | NO–FeP-his-Au | Doublet | 8.20 | −2780.851 29 |
| **D**$_3$-his | 6C | $O_2$–FeP-his-Au | Singlet | 9.67 | −2801.231 20 |

TABLE III. Bond lengths and angles of the ground state structures of the ferrous porphyrin histidine (FeP-his) coordinated with CO, NO, and $O_2$.

| Molecule | Bond[a] | Å | Angle | Degrees |
|---|---|---|---|---|
| **C**-his:FeP-his | Fe–N(P) | 2.015 | | |
| | Fe–N(his) | 2.285 | | |
| **$D_1$**-his:CO–FeP-his | C–Fe | 1.781 | C–Fe–N | 179.9 |
| | Fe–N(P) | 2.016 | | |
| | Fe–N(his) | 2.038 | | |
| **$D_2$**-his:NO–FeP-his | N–Fe | 1.778 | N–Fe–N | 139.9 |
| | Fe–N(P) | 2.017 | | |
| | Fe–N(his) | 2.080 | | |
| **$D_3$**-his:$O_2$–FeP-his | O–Fe | 1.751 | O–Fe–N | 121.7 |
| | Fe–N(P) | 2.010 | | |
| | Fe–N(his) | 2.048 | | |

[a]Level of theory, B3PW91, and basis set: 6-31G* for C, N, O, H, and S; LANL2DZ for Fe and Au.

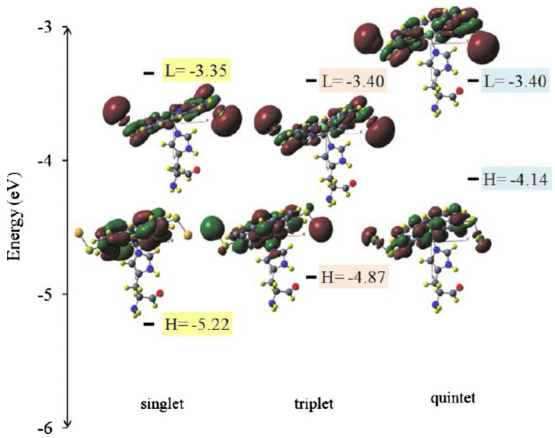


FIG. 3. (Color online) Energies of frontier orbitals in different multiplicities of ferrous five-coordinated complex, **C**-his, singlet (yellow), triplet (red), and quintet (blue). HOMO (h) and LUMO (l) energies are expressed in eV's.

Ferrous 3*d* populations, present in the 5L iron complex, have one ligand in the second shell. Interestingly the iron-nitrogen bonds show different values for the axial and equatorial ligands, i.e., a mixture of covalent and ionic bonding.[41]

The FeP-his is coordinated with NO, CO, and $O_2$ by the hybridization of the two *d* orbitals of Fe with the $\pi_g^*$ orbital of ligands, i.e., $\pi$ backbonding.[39] This coordination is related to the spin state of the complex because the electron distribution varies with the strength of the bonds to the distal ligands. Strong short bonds favor low spin and weakly paramagnetic or diamagnetic states, while weak long bonds favor high spin. Studies have shown that for neutral iron complexes, 5C is preferred to the more conventional octahedral 6C because $Fe^{+2}$ has two repulsive $e_g$ electrons which make the octahedral 6C unstable.[41] However, when NO binds to the ferrous moiety, the ferrous-histidine bond increases, weakening the bond. This effect resembles soluble guanylate cyclase spectroscopy,[42] which indicates that the binding of NO to a heme breaks the proximal histidine-iron bond, yielding a 5C complex.[43,44] However, because of the absence of the sGC enzyme, the cleavage of the Fe-histidine bond does not take place. This difference in iron coordination during NO binding assumes an important conformational role in the sGC, which is explained through a proposed pivot mechanism associated with the NO binding after the breaking of the ferrous-histidine bond.[45] Thus the six coordinated complex is an intermediate product, which is useful during sensing.

According to crystallographic data, the angles formed by the ligands are 180°, 163°, and 143° for CO, NO, and $O_2$, respectively. Table III shows the linear geometry for the CO adduct (180°) and bent for the NO (140°) and $O_2$ adducts (122°). Interestingly, these symmetry changes are detected by VCD.

According to our DFT calculations, the sensor model presents more affinity to NO ligand (Table IV). The $O_2$ binds to the sensor model, thus, it is necessary to study the interactions between the ferrous porphyrin histidine complex and the surrounding sGC enzyme, which avoids the $O_2$ interaction.[42] However, the factors that allow sGC to distinguish between NO and $O_2$ are unknown. Resonance Raman studies determinate that NO binding to sGC has been found to increase basal enzyme activity by a factor of 50–200, whereas CO binding has only a 1.4–4-fold effect.[46]

### 2. Electronic structures

The electronic structures are determined by the MO distribution, especially of the frontier orbitals, thus the calculation has to consider the multiplicity in order to find the ground state and the correct electronic configuration. Figure 3 shows HOMO and LUMO of the ferrous porphyrin histidine complex (FeP-his) with the gold atoms in orthogonal positions for different multiplicities.

Figure 4 shows the frontier orbitals obtained when the moieties CO, NO, and $O_2$ are coordinated with FeP-his. Gold atoms as electrodes are present for the current-voltage calculation.

The binding of the iron five coordinated complex with the ligands CO, NO, and $O_2$ yields their LUMOs unchanged. However, the HOMO values are reduced. Thus, the HOMO-LUMO gaps are 1.74, 1.77, and 1.82 eV, for CO, NO, and $O_2$, respectively.

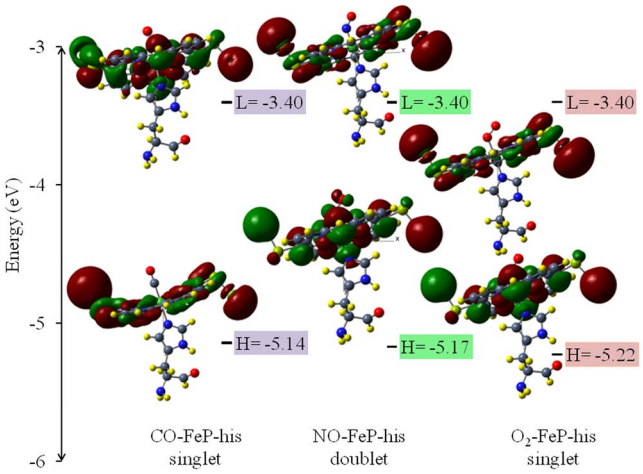


FIG. 4. (Color online) Energies of the frontier orbitals for ferrous six-coordinated complex with CO ($D_1$-his, purple), NO ($D_2$-his, green), and $O_2$ ($D_3$-his, red). HOMO (h) and LUMO (l) energies are expressed in eV's.

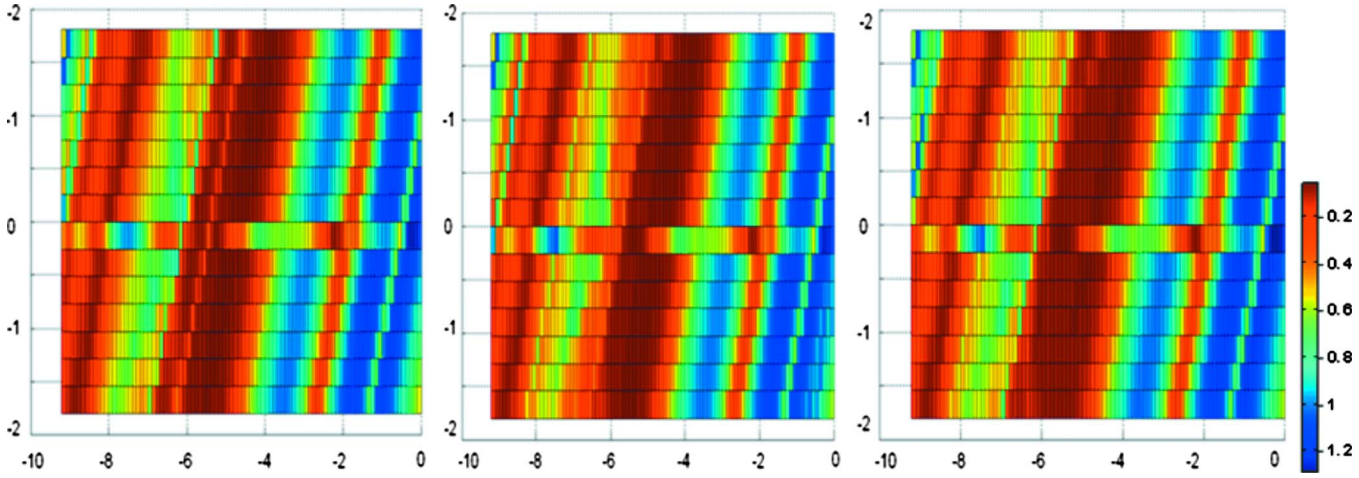


FIG. 5. (Color online) Transmission function (color coded in a scale of $\log_{10} T$) of ferrous 6 coordinated with (from left to right) carbon monoxide, nitric oxide, and dioxygen, respectively. Vertical axes are the bias voltages (volts), and horizontal axes are the energies (eV) of incoming electrons. Thus the color provides an idea of the value of the transmission function density per energy of electron per applied voltage for a given incoming electron energy at a determined bias voltage in the junction. The red color represents $10^{0.1}=1.25$ and the blue represents $10^{1.3}=20$.

### C. Detection of the sensing of NO and CO gas and its interference with $O_2$

The gases CO, NO, and $O_2$ bind with the sensor model and permit to distinguish them as target molecules. Current-voltage measurement and frequency analysis are suitable techniques to help the detection. However, the spin-coupling difference between 5L and 6L is small, but enough to distinguish them. 5L has a zigzag pattern while 6L is lineal. Therefore, all the measured information should be taken into account to establish a difference between 5C and 6C stages of the iron coordination.

#### *1. Electron transport probability*

For the electron transport probability a transmission function is calculated for the complex coordinated with CO, NO, and $O_2$. Figure 5 shows the observed voltage-energy patterns.

The transmission functions of Fig. 5 clearly show a high probability for electron transport, thus the 6C iron with CO, NO, and $O_2$ yields *I-V* curves detectable.

Figure 6 shows the HOMO and LUMO values for the FeP-his and its coordination with CO, NO, and $O_2$ for applied voltages from $-28$ to 28 V, certainly for the sake of curiosity, the behavior of the frontier MOs as voltages larger than 5 V are most likely unrealistic in this type of junctions.

#### *2. Current-voltage calculations*

Green's function-DFT allows predicting the current-voltage characteristics. Figure 7 shows the current-voltage curves for FeP-his, CO–FeP-his, NO–FeP-his, and $O_2-$FeP-his for spins up and down. The 5C iron yields an indented pattern; $\alpha$-spin shows more marked steps than $\beta$-spin. The 6C iron yields a single smooth curve superimposed to the $\alpha$-spin and $\beta$-spin.

The current-voltage curves show differences depending on the iron coordination, the 5C and 6C. The high-spin 5C iron shows Coulomb blockade at higher bias voltage. The negative differential resistant (NDR) devices behavior is explained by the analysis of frontier orbitals in the bias voltage window showed in Fig. 6. Note that the HOMO and LUMO of FeP-his complex for $\alpha$-spin and $\beta$-spin split and have zigzag patterns, which yields reduction and expansion of the HOMO-LUMO gap when a voltage is applied. Figures 6(b)–6(d) show the similitude in patterns and frontier orbital values of FeP-his coordinated with CO, NO, and $O_2$ for $\alpha$ and $\beta$ spins, thus their *I-V* curves are over among them. Recently NDR was studied in modified porphyrins;[47] however, in this work, we show the behavior in ferrous porphyrin histidine complex.

The six-coordinated iron current-voltage curve is almost the arithmetic average of the five-coordinated one. Figure 7 shows that the steady state of the 5C after the application of each electric field is shaggier than that of the 6C complex; making the 5C curve zigzag shaped. There is a difference between the 5C at the different spin-coupling state that does

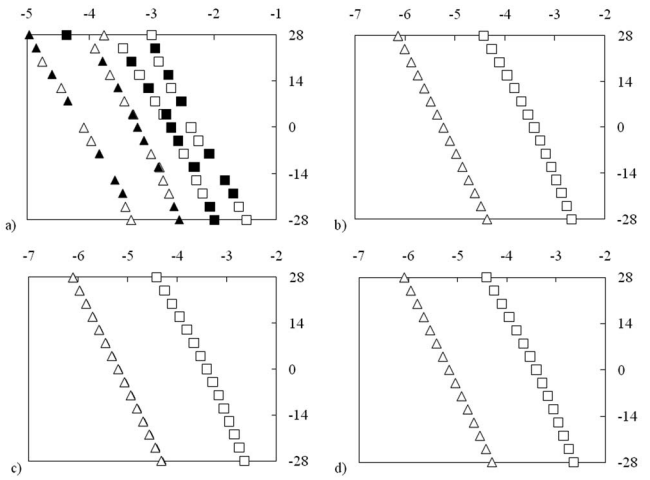


FIG. 6. Frontier orbital energies of (a) FeP-his (**C**-his), (b) CO–FeP-his ($\mathbf{D}_1$-his), (c) NO–FeP-his ($\mathbf{D}_2$-his). and (d) $O_2-$FeP-his ($\mathbf{D}_3$-his) with gold atoms in orthogonal position for bias voltages from $-28$ Vto 28V. (a) $\alpha$-spin (open) and $\beta$-spin (solid). [(a)–(d)] HOMOs (triangles) and LUMOs (squares). The veritcal axis represents the applied bias voltage (volt) and the horizontal axes represent the energy (eV).

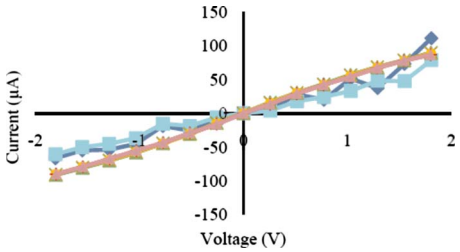


FIG. 7. (Color online) Current-voltage characteristics. Curve (5C) of triplet FeP-his (blue, $\alpha$-spin, and light blue, $\beta$-spin). Curves (6C) of singlet CO–FeP-his, doublet NO–FeP-his, and singlet $O_2$–FeP-his for $\alpha$-spin and $\beta$-spin are indistinguishable in the red straight line.

not exist in any of the 6C under study; which could be used in devices capable to detect the spin transport through an electrical signal.

This result confirms the role of the coordination to current voltage characteristic, thus the binding to a sixth ligand is important in order to get electronic stability. Reports of the effect of axial ligand in FeP-imidazole complex have shown large changes in conductance when the complex is coordinated with CO.[14] However, our study shows a striking Coulomb blockade behavior for the five-coordinated iron, and among CO, NO, and $O_2$ ligands, the conductance is very similar.

We propose the use of current-voltage measurement as the first step to test the reliability of the sensor. It permits us to know the coordinated iron state. Then the use of spectroscopy techniques to discriminate among several ligands, in order to distinguish which ligand is coordinated.

### 3. Frequency analysis

The vibrational modes represent the signature of the molecules, thus their analyses are needed for the detection process. Using DFT, it is possible to predict several spectra such as IR, Raman, VCD, and nuclear magnetic resonance (NMR) spectra, among others. However, theoretical calculations also yield some residual errors because of anharmonic behavior, solvent effects, etc.

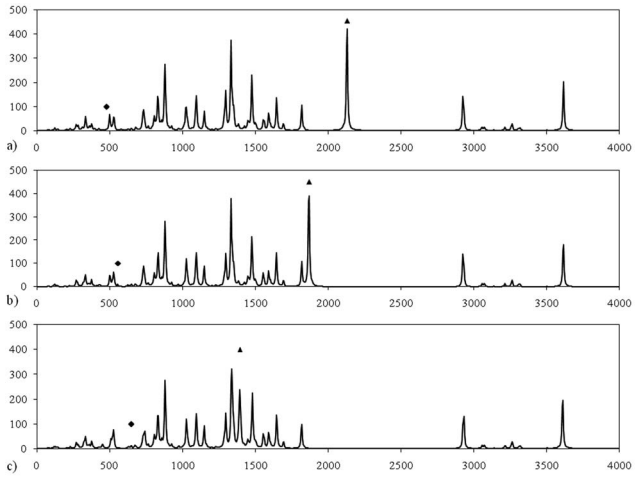


FIG. 8. IR spectrum of ferrous six-coordinated, with (a) nitric oxide, (b) carbon monoxide, and (c) molecular oxygen. The rhombic and triangle dots show the stretching vibration of Fe-ligand and the atoms of the ligands, respectively. Horizontal axes frequencies in $cm^{-1}$, and vertical axes intensities in Km/mol.

TABLE IV. Binding energy of carbon monoxide, nitric oxide, and molecular oxygen to ferrous porphyrin histidine with gold atoms in orthogonal positions (FeP-his-Au).

| | | Binding energy (kcal/mol) |
|---|---|---|
| $D_1$-his | CO–FeP-his-Au | −18.67 |
| $D_2$-his | NO–FeP-his-Au | −136.42 |
| $D_3$-his | $O_2$–FeP-his-Au | −22.84 |

The quality of the calculation is based on comparisons with experimental IR spectra of stretching and bending vibrational modes of Fe–CO, Fe–NO, and Fe–$O_2$ as well as C–O, N–O, and O–O. Comparisons are needed in order to demonstrate the quality of the theoretical spectra prediction. Figure 8 shows the theoretical prediction of IR spectrum, and Table V the comparison of theoretical and experimental vibrational stretching and bending modes in the IR spectrum.

The theoretical frequencies overestimate experimental data of the IR spectra for ferrous porphyrin histidine in 1%–5% due to basis set incompleteness, anharmonicity, solvent effects, and experimental error. Nevertheless, our DFT geometry using the combined 6-31G* and LANL2DZ basis sets resembles quite well the experimental data. Figure 9 shows the curves of VCD, infrared, and Raman spectra for the interference of CO, NO, and $O_2$ with ferrous porphyrin histidine (Table VI). Interestingly, the VCD spectra show important divergences among the CO, NO, and $O_2$ ligands. Electronic circular dichroism predictions based on DFT have been studied for the electronic analysis of porphyrin.[50] The goal is to analyze the possible interferences of $O_2$ and to select the adequate technique that allows distinguishing its presence in contrast to the CO and NO target molecules. VCD spectra are shown in Fig. 10.

The presence of the stretching Fe-ligand coordination shows the efficient molecular recognition of the system. Raman spectroscopy presents differences between the experimental data for $\upsilon$ (N–O) mode[49] and the theoretical, 1677 and 1878 $cm^{-1}$, respectively. Table VI shows the comparison of IR, Raman, and VCD signal in the stretching Fe-ligands and between the atoms of the ligands.

Stretching modes in IR, Raman, and VCD spectra are easily identifiable for ligand atoms than for Fe-ligand. There

TABLE V. Comparison between the theoretical and experimental IR frequency for stretching ($\upsilon$) and bending ($\delta$) modes of ferrous six-coordinate with carbon monoxide (Fe–CO), nitric oxide (Fe–NO), and dioxygen ($O_2$).

| | Frequency theoretical ($cm^{-1}$) | Frequency experimental ($cm^{-1}$) | Reference |
|---|---|---|---|
| $\upsilon$(Fe–CO) | 477 | 472 | 42 |
| $\delta$(Fe–C–O) | 578 | 562 | 42 |
| $\upsilon$(Fe–NO) | 556 | 520–525 | 48 and 49 |
| $\delta$(Fe–N–O) | 413 | ⋯ | |
| $\upsilon$(Fe–$O_2$) | 647 | ⋯ | |
| $\delta$(Fe–O–O) | 453 | ⋯ | |

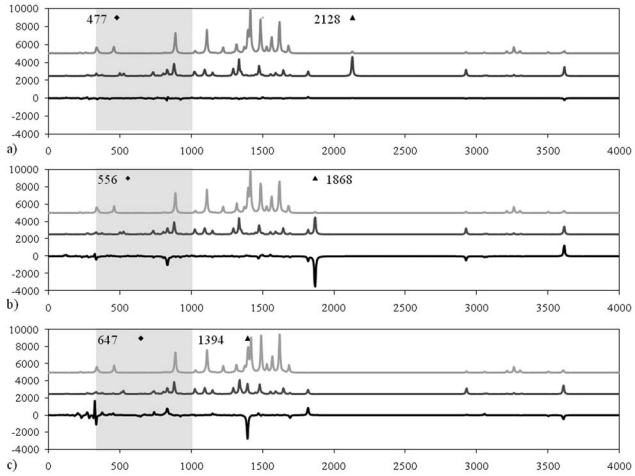


FIG. 9. Raman, infrared, and VCD of ferrous porphyrin histidine coordinated with (a) CO, (b) NO, and (c) $O_2$. Horizontal axes represent frequencies in $cm^{-1}$ and for Raman spectrum (upper trace); vertical axes is activity expressed in ($A^4$/amu). Infrared spectrum (middle trace), vertical axes are intensities expressed in (km/mol). VCD (bottom trace), vertical axes are the rotational strength expressed in ($10^{-44}$ esu$^2$ cm$^2$). The IR spectrum is moved up 2500 units and the Raman spectrum 5000 units. VCD signatures are amplified in two times on the y-axes. The rhombic dots show the stretching vibrational modes of the ferrous-ligand, and triangle dots represent the stretching vibrational modes between the atoms of the ligands. Gray regions show the stretching of Fe-ligands.

is a clear relationship between the IR and Raman signals in the stretching regions of the ligand atoms; however, the relationship for Fe-ligands is less clear. This difference could be due to the freedom in motion of the ligand atoms which cause a strong divergence of the dipole moment; instead the vibration of ferrous-ligand is weak because of its coordination with other five ligands.

In the spectrum regions of the Fe-ligand stretching vibrations, VCD spectra show identifiable signatures among the ligands in study (Fig. 9). This result is useful for the sensing/detection. Analyzing the Fe-ligand stretching region (around 700 $cm^{-1}$), it is observed for $\upsilon$ (Fe–CO) an inactive signal, while for $\upsilon$ (Fe–NO) and $\upsilon$ (Fe$-O_2$) an opposite tendency in the rotational strength occurs. Since the circularly polarized light corresponds to the infrared region, the comparison between the peaks of ligand atoms stretching in VCD spectra corresponds to intense IR bands. This correlation is lost for CO–FeP-his because its high symmetry causes similar absorbance of right and left polarized lights.

Figure 10 shows the VCD spectra, which is sensitive to the symmetry of the ligand field around the transition-metal ion. When the ligand binds to the 5C complex, a low-lying

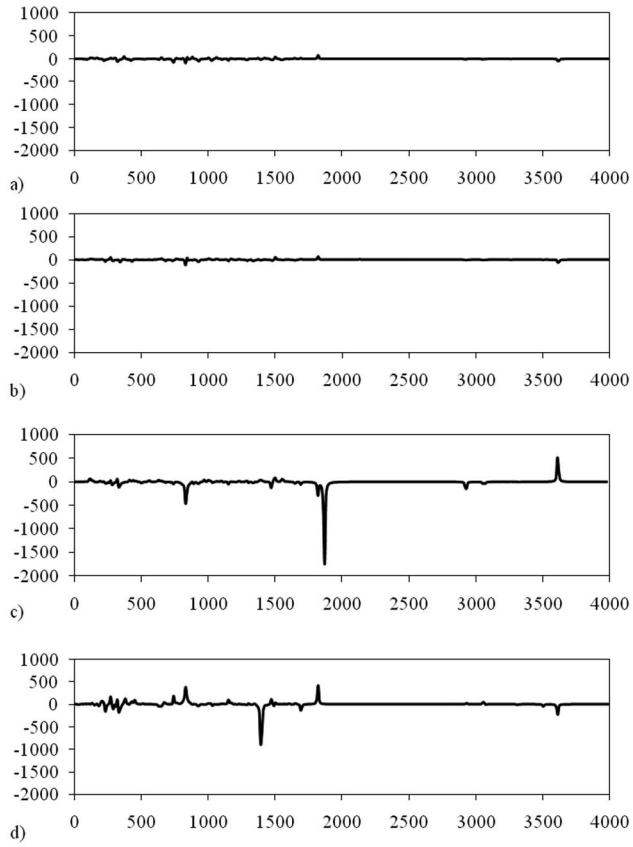


FIG. 10. VCD spectra of (a) FeP-his, (b) CO–FeP-his, (c) NO–FeP-his, and (d) $O_2$–FeP-his. Vertical axes are the rotational strengths reported in $10^{-44}$ esu$^2$ cm$^2$ and horizontal axes are the frequencies reported in $cm^{-1}$.

electronic state disappears, and degenerated *d* orbitals split according with their symmetry, thus the electric dipole and magnetic dipole change.

## IV. CONCLUSIONS

We show an example of using a biological molecule and its properties to build a sensor with the ability to detect several ligands as it takes place in their natural environment. Ferrous porphyrin histidine complex (FeP-his) properties are conserved and its responses to pollutant gases are readily trapped by the ferrous atom in 5C to 6C coordination; the ferrous is coordinated to small diatomic gases NO, CO, and $O_2$. The gas detection is achieved by electrical signals and complemented with spectroscopic techniques. The difference in the spin and electrical behaviors of the 5C and 6C is shown in the current-voltage curve. Among the 6C struc-

TABLE VI. Theoretical harmonic frequencies ($cm^{-1}$), IR intensities (km/mol), Raman activities ($A^4$/amu), depolarization ratios, dipole strengths ($10^{-40}$ esu$^2$ cm$^2$), and rotational strengths ($10^{-44}$ esu$^2$ cm$^2$) of the FeP-his coordinated with CO, NO, and $O_2$.

| Stretching ($\upsilon$) | Frequency | IR intensity | Raman activity | Depolarization ratio | Dipole strength | Rotational strength |
|---|---|---|---|---|---|---|
| $\upsilon$(Fe–CO) | 477 | 1.93 | 5.085 | 0.66 | 0.79 | −0.34 |
| $\upsilon$(Fe–NO) | 556 | 7.74 | 30.22 | 0.21 | 0.35 | 42.24 |
| $\upsilon$(Fe–$O_2$) | 647 | 1.10 | 36.80 | 0.13 | 0.24 | −161.47 |
| $\upsilon$(C–O) | 2128 | 474.15 | 236.60 | 0.56 | 0.72 | 12.33 |
| $\upsilon$(N–O) | 1868 | 469.74 | 144.34 | 0.64 | 0.78 | −2110.07 |
| $\upsilon$(O–O) | 1394 | 234.25 | 667.48 | 0.43 | 0.60 | −1377.80 |

tures, CO–FeP-his, NO–FeP-his, and $O_2$–FeP-his yield structural changes that are observed in the vibration circular dichroism, infrared, and Raman spectra, making the biosensor suitable to discern atmospheric pollutants and oxygen interference. The structural angular differences between ferrous and diatomic ligands in CO–FeP-his, NO–FeP-his, and $O_2$–FeP-his complexes are clearly detectable through VCD spectra, which result susceptible to conformational changes. The CO–FeP-his shows almost no activity in the VCD spectrum because a linear Fe–C–O arrangement. Therefore, this ligand does not break the symmetry. NO–FeP-his and $O_2$–Fe–P-his yield angles of 139.9° and 121.7°, respectively, that break the initial symmetry causing notable signals in the VCD spectra and perfectly distinguishable between them.

These structures make a junction with a gold atom in the orthogonal position with one electrode upward and the other downward with respect to the porphyrin. However, there are several places where the thiol group can be attached.

## ACKNOWLEDGMENTS

We acknowledge financial support from the U.S. Army Research Office, projects W911NF-06-1-0231 and W91NF-07-1-0199 and the U.S. Defense Threat Reduction Agency (DTRA), as well as, from the Department of Energy/Basic Energy Sciences (Grant No. DE-FG02-05ER15729).

[1] B. Weinberger, D. L. Laskin, D. E. Heck, and J. D. Laskin, Toxicol. Sci. **59**, 5 (2001).
[2] D. A. Wink and J. B. Mitchell, Free Radic. Biol. Med. **34**, 951 (2003).
[3] T. L. Poulos, Curr. Opin. Struct. Biol. **16**, 736 (2006).
[4] V. G. Kharitonov, M. Russwurm, D. Magde, V. S. Sharma, and D. Koesling, Biochem. Biophys. Res. Commun. **239**, 284 (1997).
[5] Y. Zhao, P. E. Brandish, D. P. Ballou, and M. A. Marletta, Proc. Natl. Acad. Sci. U.S.A. **96**, 14753 (1999).
[6] B. M. Leu, N. J. Silvernail, M. Z. Zgierski, G. R. A. Wyllie, M. K. Ellison, W. R. Scheidt, J. Zhao, W. Sturhahn, E. E. Alp, and J. T. Sage, Biophys. J. **92**, 3764 (2007).
[7] M. P. Johansson, D. Sundholm, G. Gerfen, and M. Wikstrom, J. Am. Chem. Soc. **124**, 11771 (2002).
[8] X.-B. Shao, X.-K. Jiang, X.-Z. Wang, Z.-T. Li, and S.-Z. Zhu, Tetrahedron **59**, 4881 (2003).
[9] G. A. Kumar, V. Thomas, G. Jose, N. V. Unnikrishnan, and V. P. N. Nampoori, Mater. Chem. Phys. **73**, 206 (2002).
[10] F. Lerouge, G. Cerveau, R. J. P. Corriu, C. Stern, and R. Guilard, Chem. Commun. (Cambridge) **15**, 1553 (2007).
[11] C. M. Drain, F. Nifiatis, A. Vasenko, and J. D. Batteas, Angew. Chem., Int. Ed. **37**, 2344 (1998).
[12] D. Gatteschi, Nature Mater. **6**, 471 (2007).
[13] V. Iancu, A. Deshpande, and S.-W. Hla, Nano Lett. **6**, 820 (2006).
[14] Y. Chen, A. Prociuk, T. Perrine, and B. D. Dunietz, Phys. Rev. B **74**, 245320 (2006).
[15] A. Mammana, M. D. Napoli, R. Lauceri, and R. Purrello, Bioorg. Med. Chem. **13**, 5159 (2005).
[16] M. J. Frisch, G. W. Trucks, H. B. Schlegel *et al.*, GAUSSIAN-2003, Revision C.2, Gaussian, Inc., Pittsburgh, PA, 2003.
[17] A. D. Becke, J. Chem. Phys. **104**, 1040 (1996).
[18] J. P. Perdew, K. Burke, and Y. Wang, Phys. Rev. B **54**, 16533 (1996).
[19] J. P. Perdew and Y. Wang, Phys. Rev. B **45**, 13244 (1992).
[20] J. P. Perdew, K. Burke, M. Ernzerhof, Phys. Rev. Lett. **77**, 3865 (1996).
[21] C. Peng, P. Y. Ayala, H. B. Schlegel, and M. J. Frisch, J. Comput. Chem. **17**, 49 (1996).
[22] P. J. Hay, and W. R. Wadt, J. Chem. Phys. **82**, 299 (1985).
[23] S. Chiodo, N. Russo, and E. Sicilia, J. Chem. Phys. **125**, 104107 (2006).
[24] F. Jensen, *Introduction to Computational Chemistry* (Wiley, NY 1999).
[25] A. D. Buckingham, Faraday Discuss. **99**, 1 (1994).
[26] J. R. Cheeseman, M. J. Frisch, F. J. Devlin, and P. J. Stephens, Chem. Phys. Lett. **252**, 211 (1996).
[27] F. J. Devlin, P. J. Stephens, J. R. Cheeseman, and M. J. Frisch, J. Am. Chem. Soc. **118**, 6327 (1996).
[28] J. M. Seminario and L. Yan, Int. J. Quantum Chem. **102**, 711 (2005).
[29] J. C. Sotelo and J. M. Seminario, J. Chem. Phys. **128**, 204701 (2008).
[30] J. M. Seminario, C. E. De La Cruz, and P. A. Derosa, J. Am. Chem. Soc. **123**, 5616 (2001).
[31] P. A. Derosa and J. M. Seminario, J. Phys. Chem. B **105**, 471 (2001).
[32] E. J. Bautista, L. Yan, and J. M. Seminario, J. Phys. Chem. C **111**, 14552 (2007).
[33] L. Yan, E. J. Bautista, and J. M. Seminario, Nanotechnology **18**, 485701 (2007).
[34] D. O. Ortiz and J. M. Seminario, J. Chem. Phys. **127**, 111106 (2007).
[35] C. Roetti, "The CRYSTAL Code," in *Quantum-Mechanical Ab-initio Calculation of the Properties of Crystalline Materials*, Vol. 67, edited by C. Pisani (Springer-Verlag, Berlin, 1996), pp. 125–137.
[36] J. C. Sotelo, L. M. Yan, M. Wang, and J. M. Seminario, Phys. Rev. A **75**, 022511 (2007).
[37] L. M. Yan and J. M. Seminario, Int. J. Quantum Chem. **107**, 440 (2007).
[38] J. M. Seminario, L. Yan, and Y. Ma, in *Chemical and Biological Standoff Detection III*, edited by J. O. Jensen and J. M. Theriault (SPIE, Boston-MS, 2005), Vol. 5995, pp. 230–244.
[39] H. Nakanishi, K. Miyamoto, M. Y. David, E. S. Dy, and R. T. a. H. Kasai, J. Phys.: Condens. Matter **19**, 365234 (2007).
[40] T. G. Spiro, Nat. Chem. Biol. **1**, 6 (2005).
[41] M. R. A. Blomberg and P. E. M. Siegbahn, Theor. Chem. Acc. **97**, 72 (1997).
[42] G. Deinum, J. R. Stone, G. T. Babcock, and M. A. Marletta, Biochemistry **35**, 1540 (1996).
[43] P. Pellicena, D. S. Karow, E. M. Boon, M. A. Marletta, and J. Kuriyan, Proc. Natl. Acad. Sci. U.S.A. **101**, 12854 (2004).
[44] D. M. Lawson, C. E. M. Stevenson, C. R. Andrew, and R. R. Eady, EMBO J. **19**, 5661 (2000).
[45] X. Ma, N. Sayed, A. Beuve, and F. v. d. Akker, EMBO J. **26**, 578 (2007).
[46] C. R. Andrew, E. L. Green, D. M. Lawson, and R. R. Eady, Biochemistry **40**, 4115 (2001).
[47] M.-Q. Long, K.-Q. Chen, L. Wang, W. Qing, B. S. Zou, and Z. Shuai, Appl. Phys. Lett. **92**, 243303 (2008).
[48] M. Negrerie, S. G. Kruglik, J.-C. Lambry, M. H. Vos, J.-L. Martin, and S. Franzen, J. Biol. Chem. **281**, 10389 (2006).
[49] E. R. Derbyshire, A. Gunn, M. Ibrahim, T. G. Spiro, R. D. Britt, and M. A. Marletta, Biochemistry **47**, 3892 (2008).
[50] J. Sÿebek and P. Bour, J. Phys. Chem. A **112**, 2920 (2008).